

by the surface tension gradient, the surface of the heat exchanger is renewed (23), thus enhancing heat flux through it. Figure 4 compares the heat transfer coefficients of the steam side of the heat exchanger under two situations: filmwise condensation on a horizontal unmodified surface and dropwise condensation on the gradient surface (24). The surface treatment enhances the heat transfer by a factor of 3 when the surface is subcooled (ΔT) from that of steam by about 20° and by a factor of 10 when subcooling is about 2°.

This methodology is also applicable on vertical surfaces, where the surface tension forces can be used in conjunction with gravity. This concept was demonstrated by preparing a 1D periodic gradient on a silicon wafer by diffusion-controlled silanization. Here the condensing drops are propelled from the hydrophobic zones and accumulate in the narrow hydrophilic channels to ultimately drain down because of gravity (25). A comparison has been made between such a drop removal mechanism and the usual method of promoting dropwise condensation by adding a surfactant (such as oleylamine) in the steam or hydrophobizing the surface by an organic coating (such as by silanization). Both the above methods yielded similar heat transfer coefficients [Nusselt number (Nu) \sim 1300], whereas the gradient surface under similar operating conditions exhibited a higher heat transfer coefficient ($Nu = 2750$). Clearly, surface tension forces can enhance the effectiveness not only of horizontal heat exchangers but of vertical heat exchangers as well. A heat exchanger surface possessing a periodic gradient has the additional advantage that its size can be scaled up in both horizontal and vertical directions without compromising the benefits of the gradient.

The phenomenon described here could also be useful in other types of heat transfer problems involving two-phase flow, an example of which is capillary force-driven thermosiphoning in heat pipes. A capillary force-driven heat pipe (26) consists of a closed container that has a heating and a cooling section. A fluid is thermally evaporated in the heating section, the vapor of which flows to the cooling section and condenses. The condensed fluid returns to the heating section by capillary action. The circulation of fluid and the corresponding heat transfer thus created within the heat pipe have a wide range of applications, including temperature stabilization in aerospace situations, thermosiphoning in Rankine engines, removal of heat from integrated microelectronic chips and controlled cooling of human body parts during cryogenic surgery. The standard way of pumping a fluid from the condensation to the evaporation section uses a wicking material, which is placed against the inner wall of the heat pipes. It is possible that the capillary pumping inside a heat pipe can be facilitated by designing a surface tension gradient in its inner wall.

References and Notes

1. D. Edwards, H. Brenner, D. Wasan, *Interfacial Transport Processes and Rheology* (Butterworth-Heinemann, Boston, 1991).
2. M. Grunze, *Science* **283**, 41 (1999).
3. M. A. Burns et al., *Proc. Natl. Acad. Sci. U.S.A.* **93**, 5556 (1996).
4. B. S. Gallardo et al., *Science* **283**, 57 (1999).
5. T. Ondarcuhu, M. Veyssie, *J. Phys. (Paris) II* **1**, 75 (1991).
6. M. K. Chaudhury, G. M. Whitesides, *Science* **256**, 1539 (1992).
7. K. Ichimura, S.-K. Oh, M. Nakagawa, *Science* **288**, 1624 (2000).
8. See Web Figs. 1 and 2 (27).
9. Visit <http://www.lehigh.edu/~mkc4/movie1.mov> to view the movements of water drops condensing on a radial gradient surface in real time.
10. Measurement of these speeds is limited by the resolution of the standard video setup, which allows us to estimate the highest speed as 15 cm/s. Some preliminary experiments using high-speed video indicate that some of the drops move at speeds as high as 1.5 m/s [see Web fig. 4 (27)].
11. A. Umur, P. Griffith, *J. Heat Transfer* **87**, 275 (1965).
12. H. P. Greenspan, *J. Fluid Mech.* **84**, 125 (1978).
13. F. Brochard, *Langmuir* **5**, 432 (1989).
14. This is true when the drop size is smaller than the Laplace length and the capillary number (Ca) is much less than unity. In our case, $Ca < 10^{-3}$.
15. P. G. De Gennes, *Rev. Mod. Phys.* **57**, 828 (1985).
16. This calculation overpredicts the droplet speed somewhat, because some of the surface energy is used up in the viscous mixing of drops. More detailed calculation shows that the droplet speed resulting from binary coalescence can easily reach about 50 cm/s. With multiple coalescence, drop speed can exceed the above values.
17. The movement of the drop edge could be facilitated by a thermal gradient of the drop close to the contact line. This is likely a second-order effect, because the

fast drop motion is observed even when the substrate surface is subcooled by only about 2 K from the temperature of steam.

18. Visit <http://www.lehigh.edu/~mkc4/movie2.mov> to view the slowing down of droplet speeds as the steam is shut off.
19. H. Zhao and D. Beysens [*Langmuir* **11**, 627 (1995)] made similar observations in the context of the water vapor ($\sim 20^\circ\text{C}$) condensing on a slightly subcooled gradient surface.
20. Visit <http://www.lehigh.edu/~mkc4/movie3.mov> to view the random movement of liquid drops coalescing on a horizontal hydrophobic surface without a gradient.
21. A. Bejan, *Heat Transfer* (Wiley, New York, 1993).
22. G. Koch, D. C. Zhang, A. Leipertz, *Heat Mass Transfer* **32**, 149 (1997).
23. Visit <http://www.lehigh.edu/~mkc4/movie4.mov> to view the movements of a liquid drop on the steam side of a heat exchanger.
24. Here we performed all of the measurements at a very low steam velocity (~ 0.2 m/s) in order to minimize the effects produced by vapor shear. As is well known in the heat transfer literature and observed by us in preliminary experiments, greater heat transfer can be obtained by increasing the steam flow rate.
25. Visit <http://www.lehigh.edu/~mkc4/movie5.mov> to view the movements of drops within two channels of a 1D periodic gradient surface.
26. A. Faghri, *Heat Pipe Science and Technology* (Taylor & Francis, Washington, DC, 1995).
27. See www.sciencemag.org/cgi/content/full/291/5504/633/DC1 for details of the methods used to prepare the gradient surfaces and their characterizations.
28. Inspiring discussions with P. G. De Gennes, A. Sharma, and M. Shanahan are gratefully acknowledged. This work was funded by an NSF REU, Dow Corning, and Air Products.

26 September 2000; accepted 1 December 2000

Capture of a Single Molecule in a Nanocavity

Li-Qun Gu,^{1*} Stephen Cheley,^{1*} Hagan Bayley^{1,2†}

We describe a heptameric protein pore that has been engineered to accommodate two different cyclodextrin adapters simultaneously within the lumen of a transmembrane β barrel. The volume between the adapters is a cavity of ~ 4400 cubic angstroms. Analysis of single-channel recordings reveals that individual charged organic molecules can be pulled into the cavity by an electrical potential. Once trapped, an organic molecule shuttles back and forth between the adapters for hundreds of milliseconds. Such self-assembling nanostructures are of interest for the fabrication of multianalyte sensors and could provide a means to control chemical reactions.

One way to create functional nanostructures is to modify existing biological structures, especially multisubunit proteins. For example, the F_1 -adenosine triphosphate synthase (F_1 -ATPase) motor has been used to rotate actin filaments (1) and inorganic “nanopro-

pellors” (2). In our laboratory, a seven-subunit protein pore, staphylococcal α -hemolysin (α HL), has been modified, both noncovalently and covalently, to produce structures with a variety of properties. For example, when molecular adapters, such as cyclodextrins (CDs) (3–6) and cyclic peptides (7), are lodged within the lumen of the pore, they alter the magnitude and selectivity of ion conduction in a transmembrane potential. The adapters can also act as binding sites for guest molecules that block conduction by the pore (3, 5, 7). In addition, flexible polymers have been covalently tethered within the lu-

¹Department of Medical Biochemistry and Genetics, Texas A&M University System Health Science Center, College Station, TX 77843, USA. ²Department of Chemistry, Texas A&M University, College Station, TX 77843, USA.

*These authors contributed equally to this report.

†To whom correspondence should be addressed. E-mail: bayley@tamu.edu

men of α HL, again leading to striking alterations in its properties (8, 9).

Here, we show that two CD adapters, β CD and hepta-6-sulfato- β CD ($s_7\beta$ CD), can be lodged simultaneously within the lumen of an α HL pore that has been genetically engineered to accommodate them. The space between the adapters forms a "nanocavity" within which an organic molecule can be trapped for hundreds of milliseconds. This approach suggests a general method for controlling the access of guest molecules to a well-defined space of nanoscopic dimensions.

We used site-directed mutagenesis in combination with measurements of the pore conductance by single-channel bilayer recording to identify the binding sites of the two CDs as well as mutations in α HL that increase their binding affinity (Figs. 1 and 2). The single-channel current is diminished while a CD is bound in the lumen of the pore (3, 6). Analysis of the frequency of occurrence and duration of the binding events permits the determination of the association (k_{on}) and dissociation (k_{off}) rate constants, and hence the dissociation constant K_d , for a CD (3, 6, 10, 11). We found that

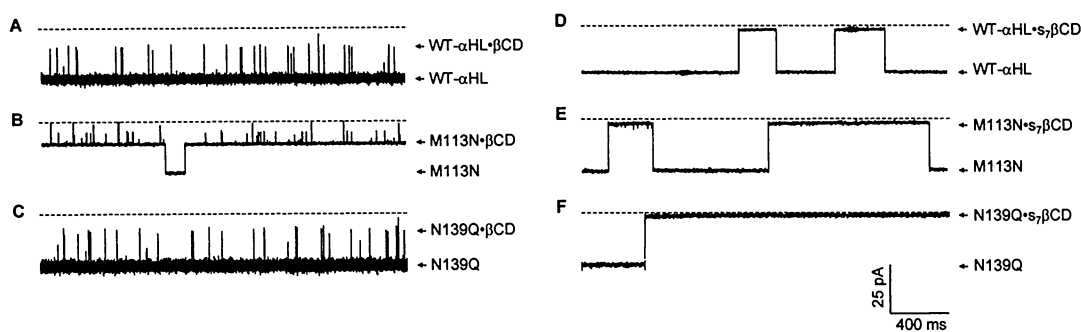
β CD resides near Met¹¹³, and that mutation to Asn at this position, in all seven subunits, increases the binding affinity for β CD by a factor of more than 10^4 (relative to wild-type α HL) under our experimental conditions (Figs. 1B and 2A). Similarly, $s_7\beta$ CD binds near Asn¹³⁹, and mutation to Gln at this position increases the binding affinity by a factor of 500 (Figs. 1F and 2A). In both cases, the decrease in K_d is mainly the result of changes in k_{off} (Fig. 2, B and C).

Because of the distance between residues 113 and 139 [C_α to C_α ~ 20 Å, vertical distance ~ 17 Å (12)], we surmised that the two adapters, β CD and $s_7\beta$ CD, bind independently of one another. The double mutant Met¹¹³ \rightarrow Asn, Asn¹³⁹ \rightarrow Gln (M113N/N139Q) in fact binds both CDs tightly (Figs. 2A and 3). β CD reduced the conductance of P_{NQ} , the pore formed by M113N/N139Q, from 668 to 285 pS (Fig. 3A), and bound with high affinity: $K_d = 3.1 (\pm 0.3) \times 10^{-7}$ M (Fig. 2A). $s_7\beta$ CD also blocked P_{NQ} , reducing the conductance to 45 pS (Fig. 3B), and bound with high affinity: $K_d = 1.6 (\pm 0.3) \times 10^{-7}$ M (Fig. 2A). When both β CD and $s_7\beta$ CD were present in the *trans* chamber (Fig. 3C), β CD was seen to bind first to P_{NQ} , reducing the conductance as expected

from 668 to 285 pS; P_{NQ} then bound $s_7\beta$ CD, which further blocked the pore and reduced the conductance to 12 pS. The 12-pS level was seen only in the presence of both CDs (13). These data enabled us to construct a molecular model (Fig. 3D) in which both β CD and $s_7\beta$ CD are lodged within the channel lumen with their molecular sevenfold axes coincident with the sevenfold axis of the pore.

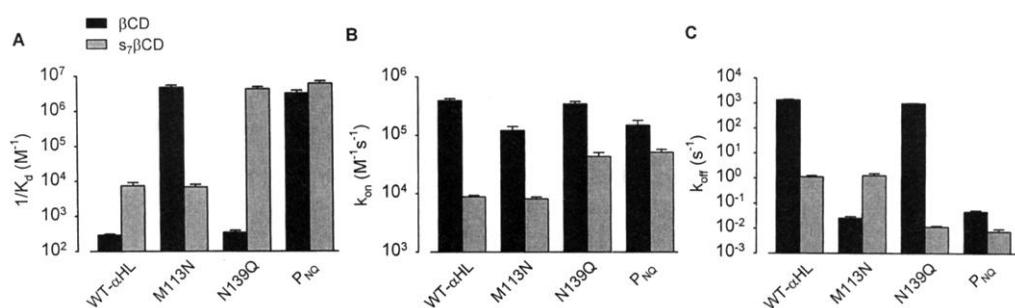
We confirmed the location of the two adapters within P_{NQ} by studying the association of guest molecules (G), which cause a further diminution of the single-channel conductance (3). At -80 mV, 1,3-adamantane dicarboxylic acid (G_1 , applied in the *cis* chamber) bound to $P_{NQ}\beta$ CD and to $P_{NQ}\beta$ CD $s_7\beta$ CD with similar dwell times, $\tau = 11$ and 8.2 ms, respectively (Fig. 4, A and C). 1-Adamantane carboxamide (G_2 , applied in the *trans* chamber) bound to $P_{NQ}s_7\beta$ CD and to $P_{NQ}\beta$ CD $s_7\beta$ CD with similar dwell times, $\tau = 250$ and 280 ms, respectively (Fig. 4, B and D). Therefore, the affinity of β CD for a guest is not perturbed by the presence of $s_7\beta$ CD, and vice versa. As predicted, $P_{NQ}\beta$ CD $s_7\beta$ CD could bind both G_1 ($\tau = 7.3$ ms) and G_2 ($\tau = 350$ ms) in the same experiment (Fig. 4E).

Fig. 1. Wild-type and mutant α HL pores with two separate binding sites for the noncovalent cyclodextrin adapters β CD and $s_7\beta$ CD. Bilayer recordings from membranes containing single α HL pores are shown. (A to C) Binding of β CD to (A) wild-type (WT), (B) M113N, and (C) N139Q α HL; (D to F) binding of $s_7\beta$ CD to (D) WT, (E) M113N, and (F) N139Q α HL. All traces were recorded at -40 mV (*cis* at ground). The chambers contained 1 M NaCl and 10 mM Na phosphate (pH 7.5). Preformed α HL heptamers were added to the *cis* chamber and 40 μ M β CD or $s_7\beta$ CD to the *trans* chamber. The traces in (A) and (C) were filtered at 5 kHz to reveal the short binding



events. The other traces were filtered at 1 kHz. For β CD [traces (A) to (C)], the dwell time of the CD is greatly increased on M113N. For $s_7\beta$ CD [traces (D) to (F)], the dwell time is increased on N139Q.

Fig. 2. Kinetic constants (A) $1/K_d$, (B) k_{on} , and (C) k_{off} from an analysis of single-channel recordings. Extended recordings were analyzed to determine k_{on} and k_{off} values for β CD and $s_7\beta$ CD, and hence K_d , for the pores formed by WT- α HL, M113N, N139Q, and M113N/N139Q (P_{NQ}) (3, 6, 10). The conditions were the same as in Fig. 1. β CD blocked WT- α HL pores from the *trans* side of the membrane, reducing the conductance from 651 pS to 240 pS (see Fig. 1) with $K_d = 3.4 (\pm 0.2) \times 10^{-3}$ M. β CD blocked the mutant M113N from the *trans* side of the membrane with $K_d = 2.1 (\pm 0.2) \times 10^{-7}$ M, reducing the conductance from 623 pS to 283 pS. Therefore, M113N binds β CD more than 10^4 times as tightly as does WT- α HL under the specified conditions. $s_7\beta$ CD reduced the conductance of WT- α HL to 53 pS with $K_d = 1.3 (\pm 0.3) \times 10^{-4}$ M. In contrast to β CD, the interaction of $s_7\beta$ CD with M113N was similar to its interaction with WT- α HL; the conductance was reduced to 51 pS and the K_d was $1.5 (\pm 0.3) \times 10^{-4}$ M. These results suggest that β CD, but not $s_7\beta$ CD, binds to α HL in the



vicinity of Met¹¹³. Mutations at Asn¹³⁹ markedly alter the affinity of $s_7\beta$ CD. N139Q bound $s_7\beta$ CD with $K_d = 2.8 (\pm 0.3) \times 10^{-7}$ M, reducing the conductance from 635 pS to 41 pS. Therefore, N139Q binds $s_7\beta$ CD more than 500 times as tightly as does WT- α HL. In contrast, N139Q and WT- α HL behaved similarly toward β CD, which reduced the conductance of N139Q to 253 pS, binding with $K_d = 2.9 (\pm 0.2) \times 10^{-3}$ M. These data suggest that $s_7\beta$ CD, but not β CD, binds in the vicinity of Asn¹³⁹. The double mutant M113N/N139Q, which forms the pore P_{NQ} , bound both CDs tightly. The main determinant of the variations in K_d was k_{off} .

REPORTS

The structure $P_{NO}\beta CD \cdot s_7\beta CD$ contains a nanocavity of $\sim 4400 \text{ \AA}^3$ for which βCD and $s_7\beta CD$ serve as gates at the *cis* and *trans* ends of the cavity, respectively (Fig. 3D). We have demonstrated the capture of G_1 within the cavity by monitoring conductance fluctuations, as shown in representative single-channel recordings (Fig. 5, A to C). The frequency of occurrence of interactions with the negatively charged G_1 , applied from the *cis* side, was maximized by carrying out the experiments at $+80 \text{ mV}$ after loading the two CDs from the *trans* side at -80 mV , conditions under which adapter binding has been examined in detail and binding of the negatively charged $s_7\beta CD$ is more rapid. When G_1 is present in the *cis* chamber, brief interactions occur with the CDs lodged in $P_{NO}\beta CD$ and $P_{NO}\cdot s_7\beta CD$, $\tau = 6.0$ and 3.9 ms , respectively (Fig. 5, A and B). When G_1 is presented to $P_{NO}\beta CD \cdot s_7\beta CD$ from the *cis* chamber, extended interactions ($\tau = 420 \text{ ms}$; Fig. 5, C and E, red) are seen as well as the short events ($\tau = 6.6 \text{ ms}$). The long events represent residency within the nanocavity. A

kinetic analysis (see below) suggests that G_1 enters the cavity through the βCD adapter, moves within the cavity from one adapter to the other, and finally exits through βCD but not through $s_7\beta CD$.

The nature of the interaction of G_1 (*cis*) with $P_{NO}\beta CD \cdot s_7\beta CD$ was consolidated by examining the voltage dependence of the kinetics (Fig. 5, D and E). The associative events (k_{on}) bear a simple relation with the transmembrane potential (ΔV) of the form $k_{on} = k_{on}(0) \exp[-z_G(1 - \delta_c^{\ddagger})\Delta V F/RT]$, where z_G is the charge on the guest, F is Faraday's constant, and δ_c^{\ddagger} is the location of the guest in the transition state with respect to the *trans* side of the membrane (10, 11). This result suggests that positive potential drives the negatively charged guest into the lumen of the pore in the expected manner (14, 15). Dissociation of G_1 (*cis*) from $P_{NO}\cdot s_7\beta CD$ also bears a simple relation with voltage (Fig. 5E), which is reasonable given that G_1 can associate with $P_{NO}\cdot s_7\beta CD$ from the *cis* and not the *trans* side of the bilayer, which in turn suggests that G_1 cannot pass through the CD

from the *cis* side. Presumably, $s_7\beta CD$ is lodged in the lumen with the sulfated face oriented toward the *trans* entrance; the seven negative charges would then repel G_1 entering from the *trans* chamber or attempting to cross from the *cis* chamber.

Events involving βCD are more complex and suggest that G_1 can bind to βCD from both sides and pass through it while it is lodged in the lumen of the pore. For $P_{NO}\beta CD$, the plots of $\log(k_{off})$ versus ΔV are curved whether G_1 is presented from the *cis* or the *trans* face (Fig. 5E). The increase in k_{off} at high positive or negative potentials suggests that G_1 can be "pushed" through the βCD adapter by the transmembrane potential. For $P_{NO}\beta CD \cdot s_7\beta CD$ with G_1 (*cis*), both long and short residencies of the guest are observed at positive potentials. The short events occur when G_1 molecules bind to βCD and dissociate from the same (*cis*) side of the bilayer. In the long events, G_1 molecules bind to βCD and are then pulled into the nanocavity under the membrane potential, where $s_7\beta CD$ acts as a stopper at the *trans* entrance. In

Fig. 3. Binding of βCD and $s_7\beta CD$ to P_{NO} . The conditions were the same as in Fig. 1 (1-kHz filter). (A and B) Binding of $40 \mu\text{M}$ βCD (A) and $40 \mu\text{M}$ $s_7\beta CD$ (B). (C) Both $40 \mu\text{M}$ βCD and $40 \mu\text{M}$ $s_7\beta CD$ were added to the *trans* side of the bilayer; βCD bound first and $s_7\beta CD$ bound second (13). (D) Molecular graphics representation of P_{NO} with both βCD and $s_7\beta CD$ bound, shown as a sagittal section along the coincident sevenfold axes of the three molecules. The locations of the two CDs are based on the mutagenesis experiments. The volume of the nanocavity between the two adapters is $\sim 4400 \text{ \AA}^3$.

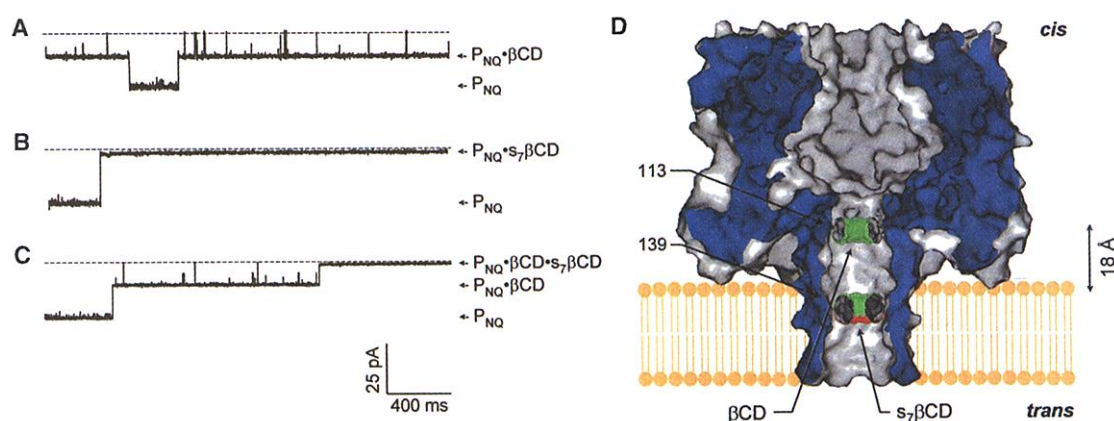
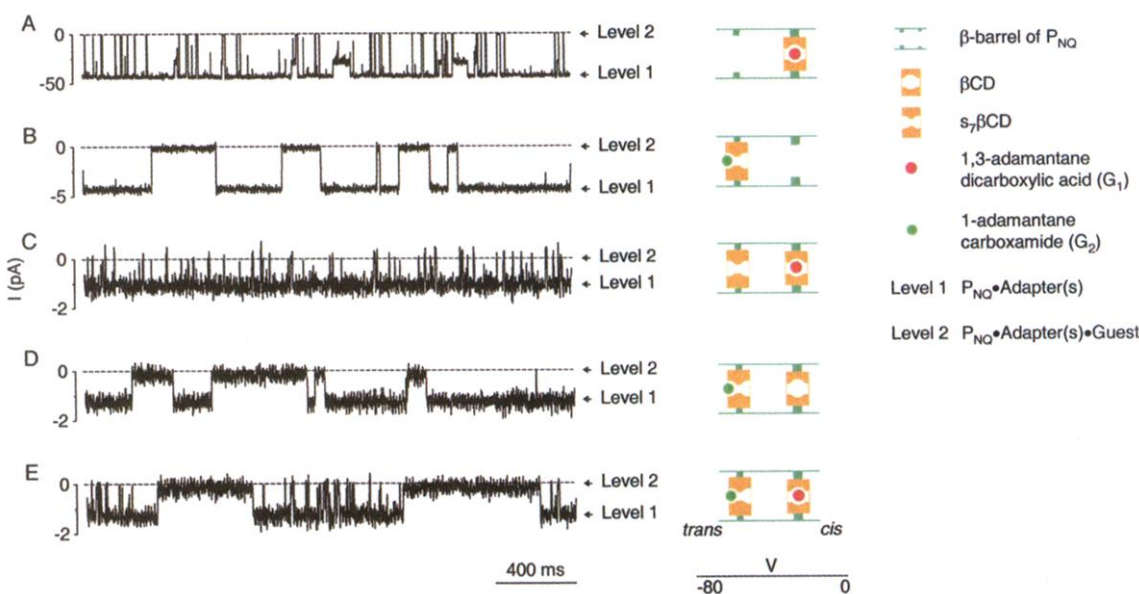


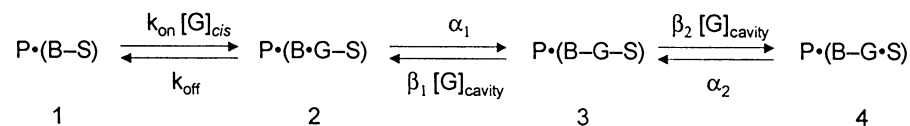
Fig. 4. Binding of guest molecules G_1 and G_2 to $P_{NO}\beta CD \cdot s_7\beta CD$. Single-channel currents were recorded at -80 mV in 2.5 M KCl and $10 \text{ mM K phosphate (pH 7.5)}$, with $40 \mu\text{M}$ βCD and/or $40 \mu\text{M}$ $s_7\beta CD$ in the *trans* chamber. (A) βCD , G_1 ($30 \mu\text{M}$, *cis*), $\tau_{off} = 11 \text{ ms}$; (B) $s_7\beta CD$, G_2 ($30 \mu\text{M}$, *trans*), $\tau_{off} = 250 \text{ ms}$; (C) βCD and $s_7\beta CD$, G_1 ($30 \mu\text{M}$, *cis*), $\tau_{off} = 8.2 \text{ ms}$; (D) βCD and $s_7\beta CD$, G_2 ($30 \mu\text{M}$, *trans*), $\tau_{off} = 280 \text{ ms}$; (E) βCD and $s_7\beta CD$, G_1 ($30 \mu\text{M}$, *cis*) and G_2 ($30 \mu\text{M}$, *trans*), $\tau_{off} = 7.3$ and 350 ms .



REPORTS

keeping with this interpretation, only short events are seen at negative potentials (Fig. 5E).

The kinetics of the interaction of G_1 with $P_{NO} \cdot \beta CD \cdot s_7 \beta CD$ are described in Scheme 1, where B is βCD and S is $s_7 \beta CD$. G_1 is bound to βCD in state 2, is resident in the cavity in state 3, and is bound to $s_7 \beta CD$ in state 4 (10). The short dwell time is represented by the trajectory $1 \rightarrow 2 \rightarrow 1$; the extended dwell time is given by $1 \rightarrow 2 \rightarrow 3 \rightarrow (2 \leftrightarrow 3 \leftrightarrow 4) \rightarrow 3 \rightarrow 2 \rightarrow 1$, where $2 \leftrightarrow 3 \leftrightarrow 4$ represents stochastic movement within the cavity. The position of G_1 within the cavity cannot be detected by current fluctuations because trapped G_1 gives almost complete current block, whether bound to βCD or $s_7 \beta CD$, and spends only a small fraction of time in solution. The kinetic analysis indicates that the probabilities of finding G_1 at various sites within the cavity at +80 mV are as follows: βCD , $P = 0.39$ (state 2); unbound, $P = 0.001$ (state 3); $s_7 \beta CD$, $P = 0.60$ (state 4). During each capture at +80 mV, G_1 transits the water-filled nanocavity a mean of 54 times, and it resides at the βCD 16 times and at the $s_7 \beta CD$ 38 times. The kinetic analysis also predicts the voltage dependence of the long dwell times (Fig. 5E)



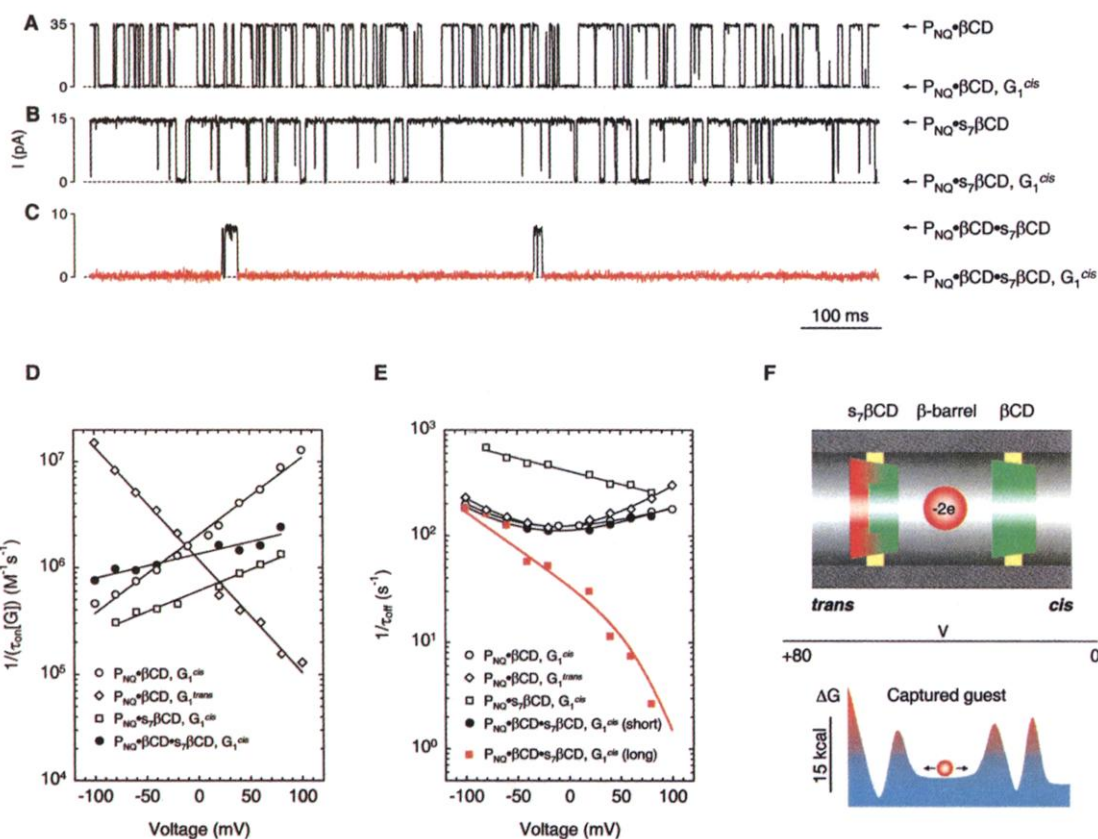
Scheme 1.

Table 1. Kinetic constants and free energies of activation for the interaction of 1,3-adamantane dicarboxylic acid (G_1) with CDs lodged within P_{NO} . Experiments were conducted at +80 mV with 2.5 M KCl and 10 mM K phosphate (pH 7.5) in both chambers and 30 μM G_1 in the *cis* or the *trans* chamber. Although most rate constants were determined for P_{NO} containing either βCD or $s_7 \beta CD$, they were in good agreement with experiment when used to describe the kinetics of $P_{NO} \cdot \beta CD \cdot s_7 \beta CD$ (Fig. 5E) (10). ΔG^\ddagger values were calculated by using Eyring's $k = (k_B T/h) \exp(-\Delta G^\ddagger/RT)$, where $k_B T/h$ was taken to be $6.15 \times 10^{12} s^{-1}$. The ΔG^\ddagger values were used to construct the free-energy profile (Fig. 5F).

Experiment	Equivalent transition in $P_{NO} \cdot \beta CD \cdot s_7 \beta CD$	Rate constant in model	Value at +80 mV	ΔG^\ddagger (kcal) at +80 mV
$P_{NO} \cdot \beta CD \cdot s_7 \beta CD$, G_1^{cis} *	$G^{cis} \rightarrow G \cdot \beta CD$	k_{on} ($M^{-1} s^{-1}$)	2.1×10^6	15 \ddagger
$P_{NO} \cdot \beta CD$, G_1^{trans} †	$G^{cis} \leftarrow G \cdot \beta CD$	k_{off} (s^{-1})	1.1×10^1	16
$P_{NO} \cdot \beta CD$, G_1^{trans} †	$G \cdot \beta CD \rightarrow G^{cavity}$	α_1 (s^{-1})	1.5×10^2	14
$P_{NO} \cdot \beta CD$, G_1^{trans} *	$G \cdot \beta CD \leftarrow G^{cavity}$	β_1 ($M^{-1} s^{-1}$)	1.6×10^5	11 \S
$P_{NO} \cdot s_7 \beta CD$, G_1^{cis} *	$G^{cavity} \rightarrow G \cdot s_7 \beta CD$	β_2 ($M^{-1} s^{-1}$)	1.3×10^6	9.8 \S
$P_{NO} \cdot s_7 \beta CD$, G_1^{cis} †	$G^{cavity} \leftarrow G \cdot s_7 \beta CD$	α_2 (s^{-1})	2.5×10^2	14

*See Fig. 5D. †See Fig. 5E. k_{off} and α_1 were determined by fitting the data to equation 4 in (10), which describes the voltage dependence of the bidirectional dissociation of a charged molecule from a site in the lumen of the pore. $\ddagger \Delta G^\ddagger$ was calculated for $[G_1]_{cis} = 30 \mu M$, the concentration of G_1 in the *cis* chamber. $\S \Delta G^\ddagger$ was calculated for $[G_1]_{cavity} = 380 mM$, the effective concentration of a single guest molecule in the nanocavity.

Fig. 5. Capture of a single molecule within the nanocavity of $P_{NO} \cdot \beta CD \cdot s_7 \beta CD$. (A to C) The interaction of G_1 with adapters lodged within the P_{NO} pore. Bilayer recordings of single channels were performed at +80 mV after loading the cyclodextrins at -80 mV. The chambers contained 2.5 M KCl and 10 mM K phosphate (pH 7.5). (A) $P_{NO} \cdot \beta CD$ and G_1 (30 μM , *cis*), $\tau_{off} = 6.0$ ms; (B) $P_{NO} \cdot s_7 \beta CD$ and G_1 (30 μM , *cis*), $\tau_{off} = 3.8$ ms; (C) $P_{NO} \cdot \beta CD \cdot s_7 \beta CD$ and G_1 (30 μM , *cis*), τ_{off} (short) = 6.6 ms, τ_{off} (long events in red, trapped) = 420 ms. (D and E) Summary of voltage dependencies of (D) $1/(\tau_{on}[G_1])$ and (E) $1/\tau_{off}$ under various conditions. In most cases, these values can be interpreted as k_{on} and k_{off} for G_1 , although the off rates may be bidirectional and the long dwells on $P_{NO} \cdot \beta CD \cdot s_7 \beta CD$ conform with a more complex function in keeping with the kinetic model (10). Open circles, $P_{NO} \cdot \beta CD$, G_1 (30 μM , *cis*); diamonds, $P_{NO} \cdot \beta CD$, G_1 (30 μM , *trans*); open squares, $P_{NO} \cdot s_7 \beta CD$, G_1 (30 μM , *cis*); solid circles, $P_{NO} \cdot \beta CD \cdot s_7 \beta CD$, G_1 (30 μM , *cis*) denote the overall k_{on} in (D) (i.e., both classes of events) or the short-dwell component in (E); solid red squares, $P_{NO} \cdot \beta CD \cdot s_7 \beta CD$, G_1 (30 μM , *cis*) denote the long-dwell component in (E). The thin lines are fitted to functions describing the voltage dependencies of the kinetics (10); the red line



in (E) is a fit to the kinetic model (10). The fit requires the use of kinetic constants obtained as described in Table 1 and their voltage dependencies (10). (F) Free-energy profile depicting the capture of a single guest molecule within the nanocavity at +80 mV. ΔG^\ddagger values were determined as described in Table 1.

and permits the construction of a free-energy profile describing residence within the cavity (Fig. 5F and Table 1).

The volume between the two adapters, $\sim 4400 \text{ \AA}^3$, is greater than that provided by most capsules synthesized by chemists (16–19). Because the size and charge of the guests can be varied, the system offers a number of possibilities for the trapping, reaction, and release of molecules. Pores containing two adapters also provide complex, highly miniaturized elements for stochastic sensing (5), which could prove advantageous for the simultaneous detection of multiple analytes (20) or could provide more distinctive signatures for individual analytes.

References and Notes

1. H. Noji, R. Yasuda, M. Yoshida, K. Kinoshita, *Nature* **386**, 299 (1997).
2. R. K. Soong *et al.*, *Science* **290**, 1555 (2000).
3. L.-Q. Gu, O. Braha, S. Conlan, S. Cheley, H. Bayley, *Nature* **398**, 686 (1999).
4. L.-Q. Gu *et al.*, *Proc. Natl. Acad. Sci. U.S.A.* **97**, 3959 (2000).
5. H. Bayley, O. Braha, L.-Q. Gu, *Adv. Mater.* **12**, 139 (2000).
6. L.-Q. Gu, H. Bayley, *Biophys. J.* **79**, 1967 (2000).
7. J. Sanchez-Quesada, M. R. Ghadiri, H. Bayley, O. Braha, *J. Am. Chem. Soc.* **122**, 11757 (2000).
8. S. Howorka *et al.*, *J. Am. Chem. Soc.* **122**, 2411 (2000).
9. L. Movileanu, S. Howorka, O. Braha, H. Bayley, *Nature Biotechnol.* **18**, 1091 (2000).
10. For experimental methods (details of the site-directed mutagenesis, pore formation, planar bilayer recording, and data analysis), a kinetic analysis of guest binding to CDs lodged in the P_{NO} pore, and tables (summary of kinetic constants for the interaction of β CD and $s_7\beta$ CD with α HL pores, and sequential binding of β CD and $s_7\beta$ CD to the P_{NO} pore), see *Science Online* (www.sciencemag.org/cgi/content/full/291/5504/636/DC1).
11. E. Moczydlowski, in *Ion Channel Reconstitution*, C. Miller, Ed. (Plenum, New York, 1986), pp. 75–113.
12. L. Song *et al.*, *Science* **274**, 1859 (1996).
13. Because β CD and $s_7\beta$ CD can only bind from the *trans* side of the bilayer and because they bind at different sites, the binding events should be ordered, β CD first, $s_7\beta$ CD second, as suggested by the example displayed (Fig. 3C). In 28 of 29 events, when β CD bound first to P_{NO} at -80 mV, the association of $s_7\beta$ CD followed. In all 28 cases, the dissociation of $s_7\beta$ CD preceded the dissociation of β CD, when the transmembrane potential was switched to $+80$ mV to shorten the dwell time of the charged adapter. In 13 events where $s_7\beta$ CD bound first to P_{NO} at 80 mV, no subsequent binding of β CD was observed (10).
14. A. M. Woodhull, *J. Gen. Physiol.* **61**, 687 (1973).
15. B. Hille, *Ionic Channels of Excitable Membranes* (Sinauer, Sunderland, MA, ed. 2, 1991).
16. D. M. Rudkevich, J. Rebeck, *Eur. J. Org. Chem.*, 1991 (1999).
17. N. Takeda, K. Umemoto, K. Yamaguchi, M. Fujita, *Nature* **398**, 794 (1999).
18. B. Olenyuk, J. A. Whiteford, A. Fechtenkötter, P. J. Stang, *Nature* **398**, 796 (1999).
19. J. Rebeck, *Chem. Commun.* **2000**, 637 (2000).
20. O. Braha *et al.*, *Nature Biotechnol.* **17**, 1005 (2000).
21. We thank O. Braha and L. Movileanu for valuable discussions. Supported by the U.S. Department of Energy, NIH, the Office of Naval Research (Multidisciplinary University Research Initiative 1999), and the Texas Advanced Technology Program.

26 September 2000; accepted 18 December 2000

The History of South American Tropical Precipitation for the Past 25,000 Years

Paul A. Baker,^{1*} Geoffrey O. Seltzer,² Sherilyn C. Fritz,³ Robert B. Dunbar,⁴ Matthew J. Grove,¹ Pedro M. Tapia,³ Scott L. Cross,¹ Harold D. Rowe,⁴ James P. Broda⁵

Long sediment cores recovered from the deep portions of Lake Titicaca are used to reconstruct the precipitation history of tropical South America for the past 25,000 years. Lake Titicaca was a deep, fresh, and continuously overflowing lake during the last glacial stage, from before 25,000 to 15,000 calibrated years before the present (cal yr B.P.), signifying that during the last glacial maximum (LGM), the Altiplano of Bolivia and Peru and much of the Amazon basin were wetter than today. The LGM in this part of the Andes is dated at 21,000 cal yr B.P., approximately coincident with the global LGM. Maximum aridity and lowest lake level occurred in the early and middle Holocene (8000 to 5500 cal yr B.P.) during a time of low summer insolation. Today, rising levels of Lake Titicaca and wet conditions in Amazonia are correlated with anomalously cold sea-surface temperatures in the northern equatorial Atlantic. Likewise, during the deglacial and Holocene periods, there were several millennial-scale wet phases on the Altiplano and in Amazonia that coincided with anomalously cold periods in the equatorial and high-latitude North Atlantic, such as the Younger Dryas.

There are three major centers of deep atmospheric convection: tropical South America, tropical Africa, and the tropical western Pacific

(1). These regions play a dominant role in energizing global atmospheric circulation through radiative and latent heating. These regions also introduce important perturbations into an otherwise more zonally uniform atmospheric circulation. Climatic variations in the tropics on interannual and interdecadal time scales affect higher-latitude climate (2) and, in turn, are influenced by higher-latitude climate (3). Because of the short duration of instrumental records and the paucity of proxy records, little is known about either the character or the causes of longer (millennial to orbital) time-scale variations in tropical climate and their

possible global teleconnections.

Here, we present data from the sedimentary record of Lake Titicaca (Bolivia and Peru) that reveal the nature of climatic variation in tropical South America during the passage from the last glacial stage through the Holocene. We postulate that the ocean-atmosphere interactions that influence modern interannual climatic variability in tropical South America also influenced climatic variability on millennial and orbital time scales.

Lake Titicaca (Fig. 1) is an important climatic archive of the late Quaternary for several reasons. It is the only large and deep freshwater lake in South America, and in deeper portions of the lake, sediment accumulated continuously for at least the past 25,000 years. By contrast, nearly all previously studied sedimentary records in the Amazon basin are lower in temporal resolution throughout and incomplete during the last glacial stage (4). Despite its high altitude (3810 m above sea level) and moderately high latitude (about 16° to 17.50°S, 68.5° to 70°W), Lake Titicaca is a reliable recorder of the precipitation that falls on a large portion of tropical South America. The annual cycle and interannual anomalies of precipitation around Lake Titicaca are correlated with those in much of Amazonia south of the equator (5). Also, modern Lake Titicaca is a nearly closed basin lake; thus, its water level, chemical composition, and biota are particularly sensitive to changes in the amount of precipitation.

The sedimentary record of Lake Titicaca has been studied previously by several workers (6–9). Because these earlier studies were conducted on cores taken in water depths <50 m, and because there was a mid-Holocene lake-level fall of 85 m (10, 11), the previously cored sequences were incomplete. Here, we present findings

¹Duke University, Division of Earth and Ocean Sciences, Durham, NC 27708, USA. ²Syracuse University, Department of Earth Sciences, Syracuse, NY 13244, USA. ³University of Nebraska, Department of Geosciences, Lincoln, NE 68588, USA. ⁴Stanford University, Department of Geological and Environmental Sciences, Palo Alto, CA 94305, USA. ⁵Woods Hole Oceanographic Institution, Woods Hole, MA 02543, USA.

*To whom correspondence should be addressed. E-mail: pbaker@geo.duke.edu